Generalized-Scattering-Matrix Modeling of Waveguide Circuits Using FDTD Field Simulations

Tsugumichi Shibata, *Member, IEEE,* and Tatsuo Itoh, *Life Fellow, IEEE*

***Abstract*— This paper presents a hybrid-analysis method for metal waveguide structures. The method is based on the generalized-scattering-matrix approach. The whole structure is divided into several components, each of which is characterized independently. Some components are analyzed using the finite-difference time-domain (FDTD) method, while the others are characterized analytically. For the FDTD simulations, we introduce a new technique for efficient and rigorous calculation of the scattering parameters. This hybrid method inherits the universality of the FDTD method and enables us to analyze larger and more complex structures using limited computer resources compared to the single FDTD analysis of a whole structure. A few results are given as examples to illustrate the validity of the method.**

***Index Terms*— Finite-difference time-domain method, hybrid-analysis method, generalized scattering matrix, waveguide circuit analysis.**

I. Introduction

THE generalized scattering matrix introduced by the group of Mittra [1], [2] is a convenient concept for solving separable waveguide structures. This concept is an extension of the ordinary scattering matrix used in circuit theory or microwave network theory, and is modified to take into account evanescent as well as propagating modes. Consequently, the obtained composite matrix is physically rigorous; it includes all necessary interactions of higher order modes between the components. The synthesis can be carried out by simple matrix calculations provided that all matrices characterizing each component of the structure are given. This paper describes the application of the generalized-scattering-matrix approach to analyses of waveguide structures, in which the finite-difference time-domain (FDTD) method is demonstrated to be usable for characterizing each component.

The time-domain methods are well known as powerful tools for three-dimensional full-wave field simulations, and have been found useful in many applications because of their universality. Since it has already been demonstrated that the modal-expansion technique works well in the analyses of metal waveguide discontinuities [3]–[5], the time-domain methods should be used effectively in conjunction with the generalized-scattering-matrix technique, especially in the application of complex waveguide structures. However, systematic demonstrations on this topic have not been reported thus far. The reason for this is that a rigorous, yet efficient, method of S-parameter calculation is not available for hybrid-mode problems in waveguide structures. Each component must be characterized accurately since an error, if any, may be accumulated and increased in the matrix calculation processes. In addition, the calculation needs to be efficient; otherwise, the usefulness of the whole approach decreases. To meet these requirements, we have proposed a new technique for S-parameter calculation using the FDTD method [6], [7]. In this paper, we will demonstrate the applicability of the proposed technique to generalized-scattering-matrix analyses of practical waveguide circuits. After reviewing the concept of the generalized scattering matrix in Section II, the new technique is described in Section III. The technique is then tested and verified numerically in Section IV, and finally, a few analysis examples are given in Section V to show the validity of the whole approach. Section VI offers some concluding remarks.

Manuscript received August 13, 1997; revised April 20, 1998.

T. Shibata is with NTT System Electronics Laboratories, Atsugi, Kanagawa 243-0198, Japan.

T. Itoh is with the Electrical Engineering Department, University of California at Los Angeles, Los Angeles, CA 90024-1594 USA.

Publisher Item Identifier S 0018-9480(98)08005-3.

II. Modeling by the Generalized Scattering Matrix

A. Generalized Scattering Matrix

Let us briefly review the concept of the generalized scattering matrix. The concept, when it was proposed, was closely related to mode-matching techniques. The original objects modeled by this matrix were the junction planes of uniform waveguides [2]. Consider a junction of two waveguides. Fig. 1 illustrates an example of an iris that consists of infinitesimally thin metal inserts in a rectangular waveguide. Now, assume that only TE_{n0} modes $(n = 1,2,3,\cdots)$ exist for simplicity, and suppose the nth mode

$$E_y^{(i)}(\boldsymbol{x},\boldsymbol{z},\omega) = \phi_n^{(i)}(\omega)\sin\left(\frac{n\pi}{a}\boldsymbol{x}\right)e^{-\gamma_n(\omega)z} \tag{1}$$

is incident upon the junction plane $(z = 0)$ from region A. The scattered field then occurs in both regions A and B, which can be expressed as follows:

$$E_y^{(r)}(\boldsymbol{x},\boldsymbol{z},\omega) = \sum_{m=1}^{\infty} A_{mn}(\omega)\phi_n^{(i)}(\omega)\sin\left(\frac{m\pi}{a}\boldsymbol{x}\right) \cdot e^{\gamma_m(\omega)z} \quad \text{in region } A \tag{2}$$

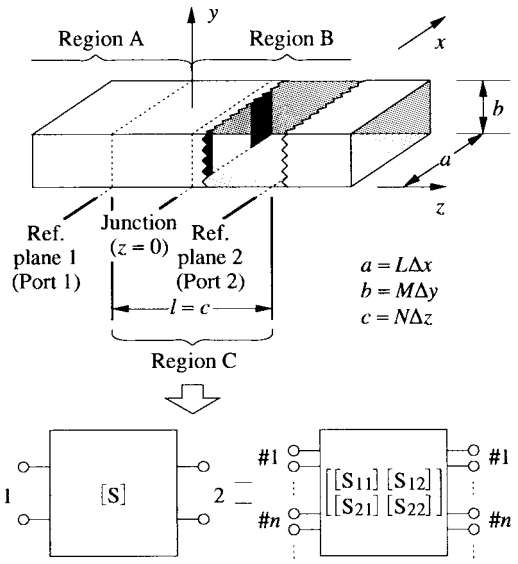

Fig. 1. An iris in a rectangular waveguide and the model of the iris obtained by the generalized scattering matrix.

$$E_y^{(t)}(\boldsymbol{x},z,\omega)=\sum_{m=1}^{\infty}B_{mn}(\omega)\phi_n^{(i)}(\omega)\sin\left(\frac{m\pi}{a}\boldsymbol{x}\right)\cdot e^{-\gamma_m(\omega)z}\quad\text{in region } B. \tag{3}$$

Using the expansion coefficients in (2) and (3), the scattering matrices at the junction are defined as

$$S_{11}=[A_{mn}(\omega)]\quad S_{21}=[B_{mn}(\omega)],\cdots. \tag{4}$$

A component, which is a scalar complex function in the conventional scattering matrix, becomes a submatrix of functions that has infinite dimensions corresponding to an infinite number of modes in the generalized scattering matrix. The junction plane is taken to be the reference plane in the original definition.

The concept of the generalized scattering matrix can be extended further in a manner that has been done in circuit theory or microwave network theory. Instead of taking the junction plane as a reference plane, a set of new reference planes (planes 1 and 2 in Fig. 1) may be taken such that the junction comes between them. This extension enables us to deal with a wider class of discontinuities. For later convenience, we call each reference plane a "physical" port and suppose that a physical port is accompanied with an infinite number of "modal" ports. The "voltage V" and "current I" at each modal port may be defined in the following way. For instance, the field on the physical port 1 (reference plane 1) may be expressed as

$$\boldsymbol{E}_t^{(\pm)}(\boldsymbol{x},\boldsymbol{y},\omega)=\sum_{n=1}^{\infty}\nu_{1,\#n}^{(\pm)}(\omega)\boldsymbol{e}_{t\#n}(\boldsymbol{x},\boldsymbol{y}) \tag{5}$$

$$\boldsymbol{H}_t^{(\pm)}(\boldsymbol{x},\boldsymbol{y},\omega)=\sum_{n=1}^{\infty}i_{1,\#n}^{(\pm)}(\omega)\boldsymbol{h}_{t\#n}(\boldsymbol{x},\boldsymbol{y}) \tag{6}$$

where $\boldsymbol{E}_t^{(\pm)}$ and $\boldsymbol{H}_t^{(\pm)}$ are the transverse components of the electric and magnetic fields, which are propagating or become evanescent toward the inside [denoted by $(-)$] or outside [by $(+)$] of discontinuity region C. $\nu_{1,\#n}^{(\pm)}$ and $i_{1,\#n}^{(\pm)}$ are the voltage and current waves defined at the modal port of the nth mode. $\boldsymbol{e}_{t\#n}$ and $\boldsymbol{h}_{t\#n}$ are the transverse-field components of the nth mode eigenfunction, which are normalized by

$$\iint|\boldsymbol{e}_{t\#n}|^2\,d\boldsymbol{S}=\iint|\boldsymbol{h}_{t\#n}|^2\,d\boldsymbol{S}=1 \tag{7}$$

respectively. The integrals in (7) are taken over the physical port and the sign of $\boldsymbol{h}_{t\#n}$ is determined such that

$$\boldsymbol{e}_{t\#n}=\boldsymbol{h}_{t\#n}\times\boldsymbol{n}_z \tag{8}$$

holds for each wave, where $\boldsymbol{n}_z$ is an unit vector normal to the physical port oriented in the direction of wave propagation or evanescence. The nodal voltage and current when the waves exist in both directions at the same time are given by

$$V_{1,\#n}=\nu_{1,\#n}^{(+)}+\nu_{1,\#n}^{(-)} \tag{9}$$

$$I_{1,\#n}=i_{1,\#n}^{(+)}-i_{1,\#n}^{(-)} \tag{10}$$

where the direction of the current is taken to be oriented toward outside the region C. The scattering matrix of region C may then be defined using the voltage waves of all modal ports as follows:

$$\begin{bmatrix}[\nu_1^{(+)}]\\ [\nu_2^{(+)}]\end{bmatrix}=\begin{bmatrix}[\boldsymbol{S}_{11}] & [\boldsymbol{S}_{12}]\\ [\boldsymbol{S}_{21}] & [\boldsymbol{S}_{22}]\end{bmatrix}\begin{bmatrix}[\nu_1^{(-)}]\\ [\nu_2^{(-)}]\end{bmatrix} \tag{11}$$

where $[\nu_i^{(-)}]$ and $[\nu_i^{(+)}]$ are the column vectors of modal voltage waves at the physical port i ($i=1$ or 2), the fields of which are propagating or become evanescent toward the inside and outside of region C, respectively.

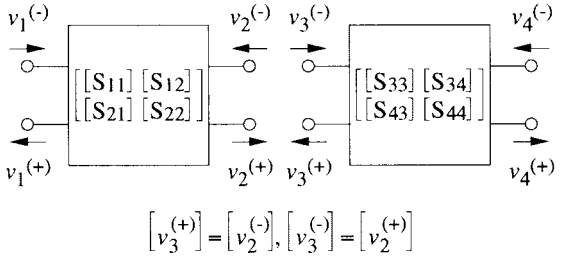

Fig. 2. Cascade connection of two generalized scattering matrices.

B. Cascade Connection of Scattering Matrices

The composite matrix of two cascaded scattering matrices can be obtained by the following matrix calculations. Consider a structure that can be separated into two parts. If both are described by the generalized scattering matrix, as shown in Fig. 2, the whole structure may also be described using a generalized scattering matrix as

$$\begin{bmatrix}[\nu_1^{(+)}]\\ [\nu_4^{(+)}]\end{bmatrix}=\begin{bmatrix}[\overline{\boldsymbol{S}}_{11}] & [\overline{\boldsymbol{S}}_{14}]\\ [\overline{\boldsymbol{S}}_{41}] & [\overline{\boldsymbol{S}}_{44}]\end{bmatrix}\begin{bmatrix}[\nu_1^{(-)}]\\ [\nu_4^{(-)}]\end{bmatrix} \tag{12}$$

where the bar on the letter $\boldsymbol{S}$ denotes that it is a composite matrix. We introduce operator $\oplus$ to indicate the cascade connection. That is,

$$\begin{bmatrix}[\overline{\boldsymbol{S}}_{11}][\overline{\boldsymbol{S}}_{14}]\\ [\overline{\boldsymbol{S}}_{41}][\overline{\boldsymbol{S}}_{44}]\end{bmatrix} = \begin{bmatrix}[\boldsymbol{S}_{11}][\boldsymbol{S}_{12}]\\ [\boldsymbol{S}_{21}][\boldsymbol{S}_{22}]\end{bmatrix} \oplus \begin{bmatrix}[\boldsymbol{S}_{33}][\boldsymbol{S}_{34}]\\ [\boldsymbol{S}_{43}][\boldsymbol{S}_{44}]\end{bmatrix} \tag{13}$$

and the submatrices of the composite matrix are formally given by

$$[\overline{\boldsymbol{S}}_{11}] = [\boldsymbol{S}_{11}] + [\boldsymbol{S}_{12}][[\boldsymbol{I}] - [\boldsymbol{S}_{33}][\boldsymbol{S}_{22}]]^{-1}[\boldsymbol{S}_{33}][\boldsymbol{S}_{21}] \tag{14}$$

$$[\overline{\boldsymbol{S}}_{14}] = [\boldsymbol{S}_{12}][[\boldsymbol{I}] - [\boldsymbol{S}_{33}][\boldsymbol{S}_{22}]]^{-1}[\boldsymbol{S}_{34}] \tag{15}$$

$$[\overline{\boldsymbol{S}}_{41}] = [\boldsymbol{S}_{43}][[\boldsymbol{I}] - [\boldsymbol{S}_{22}][\boldsymbol{S}_{33}]]^{-1}[\boldsymbol{S}_{21}] \tag{16}$$

and

$$[\overline{\boldsymbol{S}}_{44}] = [\boldsymbol{S}_{43}][[\boldsymbol{I}] - [\boldsymbol{S}_{22}][\boldsymbol{S}_{33}]]^{-1}[\boldsymbol{S}_{22}][\boldsymbol{S}_{34}] + [\boldsymbol{S}_{44}]. \tag{17}$$

For practical computations, these submatrices must be truncated to finite sizes. However, a considerably accurate result can be obtained by truncating the infinite matrices to a reasonably small size in many cases. Here, we considered parts that were cascaded by physical ports. Extension of the operation to include parts that have multiports is straightforward. We can also use these results for deembedding the termination for a physical port, or even for a particular modal port of a part. Such an example can be seen later in Sections III-B and IV-B.

III. Parameter Calculation by FDTD Simulations

The generalized scattering matrix may be used in conjunction with any kind of analysis method. Some components may be characterized analytically and others numerically. Each analysis can be carried out completely independently. By employing a universal numerical method, the scope of the generalized-scattering-matrix approach is expected to be potentially extended. In this section, a new technique is described for the calculation of the component matrix using FDTD simulations.

A. Time-Domain Modal Voltage and Current

Since FDTD simulations yield time-domain data, one must first note what the time-domain quantities look like at the modal ports that have been introduced earlier in the frequency domain. The answer to this can be derived from inverse Fourier transforms of the definitions in (5) and (6). In the most general case, eigenfunctions $\boldsymbol{e}_t$ and $\boldsymbol{h}_t$ should be assumed to be frequency-dependent. However, in such a case, obtaining frequency-domain information from the time-domain data is not very feasible because a convolution has to be performed many times. To avoid this situation, we have implicitly made an assumption on the port structure. Let us again consider region C in Fig. 1. This is a portion of a metal waveguide. The cross-sectional shape of the waveguide may actually be arbitrary. Between the physical ports there can be any kind of discontinuity as long as it can be treated by the conventional FDTD method. The only assumption we make is a lossless homogeneous structure on the ports, i.e., the waveguide must be filled with a constant medium at least at the cross section of the reference planes. The eigenfunctions of the waveguide modes defined at the ports then become frequency-independent. Therefore, from (5) and (6), we get

$$\boldsymbol{E}_t^{(\pm)}(\boldsymbol{x},\boldsymbol{y},t) = \sum_{n=1}^{\infty} \nu_{1,\#n}^{(\pm)}(t)\boldsymbol{e}_{t\#n}(\boldsymbol{x},\boldsymbol{y}) \tag{18}$$

$$\boldsymbol{H}_t^{(\pm)}(\boldsymbol{x},\boldsymbol{y},t) = \sum_{n=1}^{\infty} i_{1,\#n}^{(\pm)}(t)\boldsymbol{h}_{t\#n}(\boldsymbol{x},\boldsymbol{y}) \tag{19}$$

where $v_{1,\#n}^{(\pm)}(t)$ and $i_{1,\#n}^{(\pm)}(t)$ are inverse Fourier transforms of $v_{1,\#n}^{(\pm)}(w)$ and $i_{1,\#n}^{(\pm)}(w)$, respectively. These equations mean that the observed total field can be expressed by a linear combination of the modal eigenfunctions at any moment. Consequently, one can find the time-domain modal voltage and current at any FDTD time step from the observed field distribution on the physical port using the orthogonality between the modes, and can eventually calculate the frequency-domain modal voltage and current using fast Fourier transform (FFT).

B. New Method

When we analyze a circuit using FDTD simulations, it is necessary to terminate the circuit ports by an appropriate condition. The absorbing boundary condition (ABC), which minimizes the reflection of outgoing waves, has been widely used so far. By adopting the ABC at the boundary of the analysis region, waves reflected back from the boundary can be ignored. The S-parameters of the circuit are then usually calculated by taking the ratios of the outgoing voltage wave spectra to the incoming ones in a wide range of frequencies. However, this method includes two potentially delicate procedures: the separation of backward- and forward-going waves at the input port, and the ABC calculation to minimize undesirable reflection from the boundary. These procedures require additional computational efforts, which are not minor.

Nonreflection at the circuit ports is by no means the only condition for S-parameter calculation. A more general requirement is port termination by well-defined impedances. In this sense, the ABC is a particular case where the ports are terminated by the characteristic impedance of the waveguide, which is frequency dependent in general. Here, we consider a termination that is represented by a simple equivalent circuit. Suppose that we can terminate each modal port by a terminating impedance Z_{term}, which is different from the waveguide characteristic impedance. For simplicity, we now consider only one mode at each physical port, and examine the equivalent circuit of region C in Fig. 1. The circuit diagram of such a system is illustrated in Fig. 3, where $Z_{\mathrm{term}} = R_1$ at port 1 and $Z_{\mathrm{term}} = R_2$ at port 2. We employ the following definition for the scattering matrix of this system:

$$\begin{bmatrix}\dfrac{\nu_{1,\#i}^{(+)}(\omega)}{\sqrt{R_1}}\\ \dfrac{\nu_{2,\#j}^{(+)}(\omega)}{\sqrt{R_2}}\end{bmatrix} = \begin{bmatrix}\boldsymbol{S}_{11}[\#i,\#i](\omega) & \boldsymbol{S}_{12}[\#i,\#j](\omega)\\ \boldsymbol{S}_{21}[\#j,\#i](\omega) & S_{22}[\#j,\#j](\omega)\end{bmatrix} \cdot \begin{bmatrix}\dfrac{\nu_{1,\#i}^{(-)}(\omega)}{\sqrt{R_1}}\\ \dfrac{\nu_{2,\#j}^{(-)}(\omega)}{\sqrt{R_2}}\end{bmatrix}. \tag{20}$$

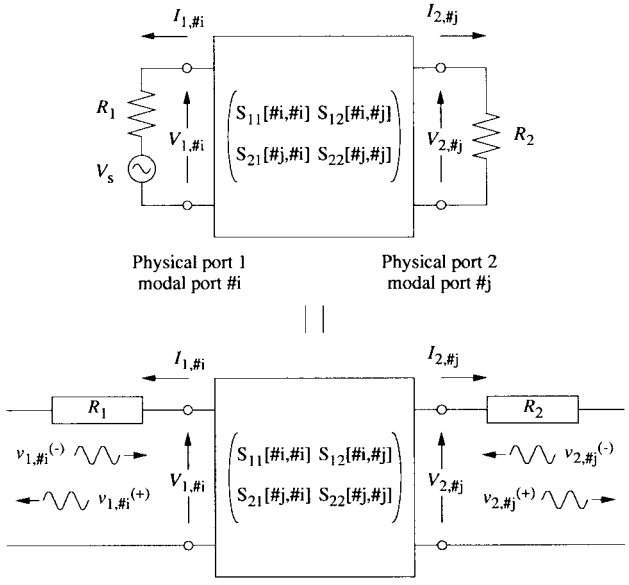

Fig. 3. An equivalent circuit of a two-port metal waveguide structure terminated by well-defined impedances.

Voltage waves $v_{1,\#i}^{(-)}$, $v_{1,\#i}^{(+)}$, $v_{2,\#j}^{(-)}$, and $v_{2,\#j}^{(+)}$ can be expressed using the nodal voltage and current at each modal port as

$$\nu_{1,\#i}^{(-)}(\omega) = \frac{V_{1,\#i}(\omega) - I_{1,\#i}(\omega)R_1}{2} \tag{21}$$

$$\nu_{1,\#i}^{(+)}(\omega) = \frac{V_{1,\#i}(\omega) + I_{1,\#i}(\omega)R_1}{2} \tag{22}$$

$$\nu_{2,\#j}^{(-)}(\omega) = \frac{V_{2,\#j}(\omega) - I_{2,\#j}(\omega)R_2}{2} \tag{23}$$

$$\nu_{2,\#j}^{(+)}(\omega) = \frac{V_{2,\#j}(\omega) + I_{2,\#j}(\omega)R_2}{2}. \tag{24}$$

In addition, the terminating condition at each port gives

$$V_{1,\#i}(\omega) - I_{1,\#i}(\omega)R_1 = V_s(\omega) \tag{25}$$

and

$$V_{2,\#j}(\omega) - I_{2,\#j}(\omega)R_2 = 0. \tag{26}$$

From (20), together with (21)–(26), one can eventually obtain

$$S_{11}[\#i,\#i](\omega) = \frac{2V_{1,\#i}(\omega) - V_s(\omega)}{V_s(\omega)} \tag{27}$$

$$S_{21}[\#j,\#i](\omega) = \sqrt{\frac{R_1}{R_2}}\, 2V_{2,\#j}(\omega). \tag{28}$$

These formulas enable us to calculate the S-parameters from only the nodal voltages [7]. Consequently, the troublesome procedure of separating the backward- and forward-going waves can be avoided. Furthermore, we do not have to worry about undesirable reflections from the terminations. There exist some intended reflections in this system; however, everything is automatically taken into account. Extension to the general case where there is a finite number of modal ports at each physical port is straightforward.

It should be noted here that the parameters defined in Section II and here differ in the two points. First, the standard impedance is obviously different. Secondly, (20) defines the S-parameters in terms of power flow $\nu/\sqrt{R} = \sqrt{v}i$, while (11) gives them in terms of voltage waves. These differences yield different numbers as the parameters for the same structure. However, of course, either set of parameters is convertible to the other. Let us denote the matrices defined in (20) by $\hat{}$, such that $[\hat{S}]$, in order to distinguish them from the matrices $[S]$ defined in (11). $[\hat{S}]$ can be converted to $[S]$ as

$$[S] = [G_{S\leftarrow\hat{S}}] \oplus [\hat{S}] \oplus [G_{\hat{S}\rightarrow S}] \tag{29}$$

where $[G_{S\leftarrow\hat{S}}]$ and $[G_{\hat{S}\rightarrow S}]$ are the conversion matrices, and are given, in the case of Fig. 3, by

$$[G_{S_{1,\#i}\leftarrow\hat{S}_{1,\#i}}] = \begin{bmatrix} \Gamma & (1-\Gamma)/\sqrt{R_1} \\ (1+\Gamma)/\sqrt{R_1} & -\Gamma \end{bmatrix}$$

$$\Gamma(\omega) = \frac{R_1 - Z_{01,\#i}(\omega)}{R_1 + Z_{01,\#i}(\omega)} \tag{30}$$

$$[G_{\hat{S}_{2,\#j}\rightarrow S_{2,\#j}}] = \begin{bmatrix} -\Gamma & (1+\Gamma)/\sqrt{R_2} \\ (1-\Gamma)/\sqrt{R_2} & \Gamma \end{bmatrix}$$

$$\Gamma(\omega) = \frac{R_2 - Z_{02,\#j}(\omega)}{R_2 + Z_{02,\#j}(\omega)} \tag{31}$$

$Z_{01,\#i}$ and $Z_{02,\#j}$ denote the characteristic impedance of each mode on physical ports 1 and 2, respectively. In general multimode cases, each component in the above conversion matrices becomes a diagonal submatrix whose dimension corresponds to the number of modes considered at each physical port.

We will next explain how to implement the terminations described above in the FDTD algorithm.

C. Impedance Boundary Condition

Consider again, region C in Fig. 1. In order to terminate port 1 with terminating impedance $Z_{\rm term}$, the following relationship is requested at every modal port on this physical port:

$$V_{1,\#n}(\omega) = Z_{\rm term}(\omega) I_{1,\#n}(\omega). \tag{32}$$

Referring to the definitions of the voltage and current, (32) can be rewritten as a relationship between the field components, which must be satisfied on the port plane. That is, using (5)–(10),

$$\boldsymbol{E}_t(x,y,\omega) = Z_{\rm term}(\omega)\boldsymbol{H}_t(x,y,\omega) \times \boldsymbol{n}_z \tag{33}$$

where $\boldsymbol{E}_t$ and $\boldsymbol{H}_t$ are the transverse components of the total field, i.e., $\boldsymbol{E}_t = \boldsymbol{E}_t^{(+)} + \boldsymbol{E}_t^{(-)}$ and $\boldsymbol{H}_t = \boldsymbol{H}_t^{(+)} + \boldsymbol{H}_t^{(-)}$. $\boldsymbol{n}_z$ is oriented toward the outside of the analysis region in this case. Alternatively, in terms of the Cartesian field components,

$$E_x(x,y,\omega) = -Z_{\rm term}(\omega) H_y(x,y,\omega) \tag{34}$$

$$E_y(x,y,\omega) = Z_{\rm term}(\omega) H_x(x,y,\omega) \tag{35}$$

for physical port 1. This condition is called the impedance boundary condition (IBC), and can be implemented in the FDTD algorithm as follows.

When we descretize the field in region C in Fig. 1 using an FDTD mesh, we have two choices in setting the mesh nodes on each physical port. The first is to adjust the mesh such that E_x-, E_y-, and H_z-nodes exist on the port plane. This case is illustrated in Fig. 4(a). The second is to adjust it such that

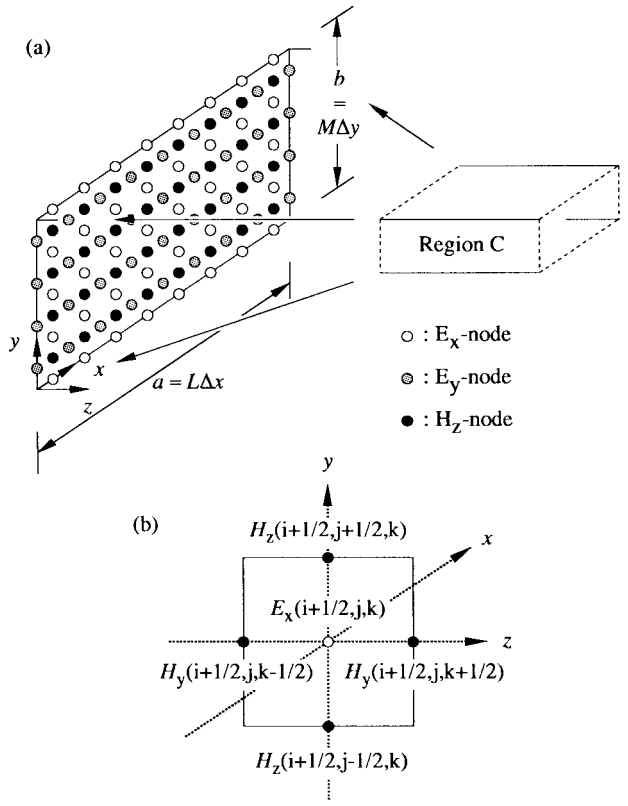

Fig. 4. An arrangement of FDTD mesh nodes on the physical port.

H_x-, H_y-, and E_z-nodes come on the plane. In the first case, the condition of the type

$$Y_{\text{term}}(\omega) = \frac{1}{Z_{\text{term}}(\omega)} = G_{\text{term}} + j\omega C_{\text{term}} \tag{36}$$

can be implemented easily. Fig. 4(b) shows an E_x-node and related neighboring H-nodes. The value of E_x can usually be updated using the values of these H-nodes. However, when the E_x node exists on physical port 1, one of the values, i.e., $H_y(i+1/2, j, k-1/2)$ in Fig. 4(b), is nonexistent. Therefore, instead of this nonexistent value, the condition in (34) may be used. Substituting (36) into (34), one can rewrite this condition into the following finite-difference form:

$$\begin{aligned} -\frac{H_y^{n-1/2}(i+1/2,j,-1/2) + H_y^{n-1/2}(i+1/2,j,1/2)}{2} \\ = G_{\text{term}}\,\frac{E_x^n(i+1/2,j,0) + E_x^{n-1}(i+1/2,j,0)}{2} \\ + C_{\text{term}}\,\frac{E_x^n(i+1/2,j,0) - E_x^{n-1}(i+1/2,j,0)}{\Delta t}. \end{aligned} \tag{37}$$

Notice here that we have used the transformation $j\omega \Leftrightarrow \partial/\partial t$, and have taken an average in space for H_y and an average in time for E_x to evaluate the values at point $[(i+1/2)\Delta x, j\Delta y, 0]$ and at time $(n-1/2)\Delta t$. Substituting (37) into the term of $H_y(i+1/2, j, -1/2)$ in the original FDTD E_x-node updating formula, we obtain the following new formula for updating the E_x nodes on physical port 1:

$$\begin{aligned} &E_x^n(i+1/2,j,0) \\ &\quad = \frac{\varepsilon_0\varepsilon_{rx} - \Delta t G_{\text{term}}/\Delta z + 2C_{\text{term}}/\Delta z}{\varepsilon_0\varepsilon_{rx} + \Delta t G_{\text{term}}/\Delta z + 2C_{\text{term}}/\Delta z} \\ &\qquad \cdot E_x^{n-1}(i+1/2,j,0) \\ &\qquad + \frac{\Delta t}{(\varepsilon_0\varepsilon_{rx} + \Delta t G_{\text{term}}/\Delta z + 2C_{\text{term}}/\Delta z)\Delta y} \\ &\qquad \cdot [H_z^{n-1/2}(i+1/2,j+1/2,0) \\ &\qquad\quad - H_z^{n-1/2}(i+1/2,j-1/2,0)] \\ &\qquad - \frac{2\Delta t}{(\varepsilon_0\varepsilon_{rx} + \Delta t G_{\text{term}}/\Delta z + 2C_{\text{term}}/\Delta z)\Delta z} \\ &\qquad \cdot H_y^{n-1/2}(i+1/2,j,1/2). \end{aligned} \tag{38}$$

Similar formulas can be deduced for the E_y nodes. By applying these formulas to every E_x and E_y node on physical port 1, all modal ports on this physical port can be terminated by the condition in (36). As easily seen, this implementation is much simpler than those of complicated ABC's. No additional memory is required and the computational steps are almost the same as those for internal nodes. If the second choice of the mesh setting is employed, an impedance type

$$Z_{\text{term}}(\omega) = R_{\text{term}} + j\omega L_{\text{term}} \tag{39}$$

can be implemented similarly.

D. Voltage Signal Source

Next, we will implement the voltage signal source for exciting a modal port. Originally, the FDTD updating formulas were directly derived from the differential form of Maxwell's curl equations. However, their integral form sometimes provides better insight into the physical meaning of the formulas. Let us examine the physical meaning of (38). Equation (38) may be rewritten as (40), shown at the bottom of this page, which can be interpreted as

$$\begin{aligned} \int_{\Delta y\times(\Delta z/2)} \frac{\partial \boldsymbol{D}}{\partial t}\cdot d\boldsymbol{S} + \int_{D\to A} \boldsymbol{n}_z \times (\boldsymbol{j}_{G\text{term}} + \boldsymbol{j}_{C\text{term}})\cdot d\boldsymbol{s} \\ = \int_{A\to B\to C\to D} \boldsymbol{H}\cdot d\boldsymbol{s}. \end{aligned} \tag{41}$$

$$\begin{aligned} &\varepsilon_0\varepsilon_{rx}\,\frac{E_x^n(i+1/2,j,0) - E_x^{n-1}(i+1/2,j,0)}{\Delta t}\,\Delta y\,\frac{\Delta z}{2} + G_{\text{term}}\,\frac{E_x^n(i+1/2,j,0) + E_x^{n-1}(i+1/2,j,0)}{2}\,\Delta y \\ &\quad + C_{\text{term}}\,\frac{E_x^n(i+1/2,j,0) - E_x^{n-1}(i+1/2,j,0)}{\Delta t}\,\Delta y \\ &\quad = H_z^{n-1/2}(i+1/2,j+1/2,0)\,\frac{\Delta z}{2} - H_y^{n-1/2}(i+1/2,j,1/2)\Delta y - H_z^{n-1/2}(i+1/2,j-1/2,0)\,\frac{\Delta z}{2} \end{aligned} \tag{40}$$

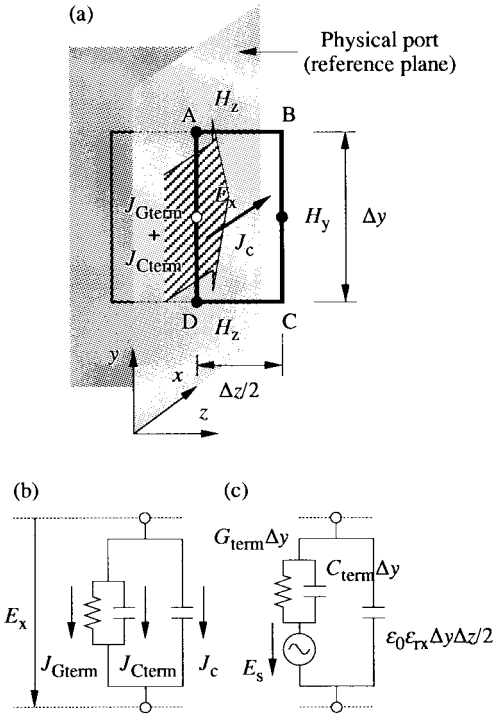

Fig. 5. Physical model of an E_x node on the physical port terminated by the impedance boundary condition of the type $Z_{\rm term}(w) = 1/(G_{\rm term} + jwC_{\rm term})$.

The first term on the left-hand side represents the displacement current J_c, which crosses the area surrounded by the path A–B–C–D–A in Fig. 5(a). The right-hand side gives a part of the loop integral (on the path A–B–C–D) of the magnetic field. And the remainder of the loop integral is given by the second term of the left-hand side in terms of surface currents $J_{G\rm term}$ and $J_{C\rm term}$ that flow on the physical port (reference plane). The magnitude of magnetic field H_y at this node should be equivalent to the total surface current $J_{G\rm term} + J_{C\rm term}$. From this interpretation, an equivalent circuit that describes the relation between J_c, $J_{G\rm term}$, $J_{C\rm term}$, and E_x can be derived, and it is represented in Fig. 5(b). An excitation term can be added to this local node by introducing electromotive force E_s into this equivalent circuit, as shown in Fig. 5(c). This modifies (40) to (42), shown at the bottom of this page, where E_s' is the time derivative of E_s. In order to excite a certain modal port, every E_x and E_y node on this physical port needs to be excited at the same time with the amplitude in proportion to the eigenfunction. Therefore, we eventually get the following excitation term, which should be added to the right-hand side of (38):

$$-\frac{2\Delta t}{(\varepsilon_0\varepsilon_{rx} + \Delta t G_{\rm term}/\Delta z + 2C_{\rm term}/\Delta z)\,\Delta z} \cdot[G_{\rm term}V_s^{n-1/2} + C_{\rm term}V_s'^{n-1/2}]e_{x\#n}(i+1/2,j). \quad (43)$$

By this term, the modal voltage source of the nth mode having internal impedance $Z_{\rm term} = 1/(G_{\rm term} + jwC_{\rm term})$ is implemented. $V_s'^{n-1/2}$ is the time derivative of the voltage $V_s^{n-1/2}$. $e_{x\#n}(i+1/2,j)$ is the value of the x component of the eigenfunction at this point. Similar formula can be deduced for the E_y-nodes.

IV. Numerical Verifications

The procedure for S-parameter calculation using the idea described in Section III is summarized below.

1) Divide a whole structure into parts that are to be modeled individually, and thereby define the physical ports for each part.
2) Find the possible modes on each physical port.
3) Build up the FDTD model by setting medium constants in the mesh.
4) Adopt the impedance boundary condition on every physical port.
5) Excite modal port #1 on physical port 1 using the voltage source $V_s(t)$. $V_s(w)$ can be calculated from $V_s(t)$ in advance.
6) Observe the electric-field distribution on all physical ports, and thereby extract the nodal voltage of every modal port at each time step.
7) Calculate Fourier transforms of all nodal voltages.
8) Obtain $\hat{S}_{11}[\#i,\#1]$ and $\hat{S}_{21}[\#j,\#1]$ for $i = 1, 2, \cdots$, and $j = 1, 2, \cdots$, using the proposed formulas.
9) Repeat (5)–(8), changing the excitation port to complete the generalized scattering matrix.

Among these steps, (4)–(8) are newly proposed in this paper. The following gives numerical verifications of the S-parameter calculation. The issue of the possible mode selection is also addressed.

A. Hollow Waveguide

Fig. 6(a) and (b) presents the frequency characteristics of S-parameters for a hollow rectangular waveguide. Having the physical ports terminated by R ($= 500\ \Omega$), $\hat{S}_{11}$ and $\hat{S}_{21}$ of the 6.508-mm-length waveguide are plotted for $\rm TE_{10}$, $\rm TE_{30}$, and $\rm TE_{\bar{3}0}$ modes, respectively. Here, the difference between the parameter sets S and $\hat{S}$ is clearly seen. Since $\rm TE_{10}$ is a propagating mode at these frequencies, the magnitudes of

$$\varepsilon_0\varepsilon_{rx}\frac{E_x^n(i+1/2,j,0) - E_x^{n-1}(i+1/2,j,0)}{\Delta t}\Delta y\,\frac{\Delta z}{2} + G_{\rm term}\left[\frac{E_x^n(i+1/2,j,0) + E_x^{n-1}(i+1/2,j,0)}{2} - E_s^{n-1/2}\right]\Delta y + C_{\rm term}\left[\frac{E_x^n(i+1/2,j,0) - E_x^{n-1}(i+1/2,j,0)}{\Delta t} - E_s'^{n-1/2}\right]\Delta y = H_z^{n-1/2}(i+1/2,j+1/2,0)\,\frac{\Delta z}{2} - H_y^{n-1/2}(i+1/2,j,1/2)\Delta y - H_z^{n-1/2}(i+1/2,j-1/2,0)\,\frac{\Delta z}{2} \quad (42)$$

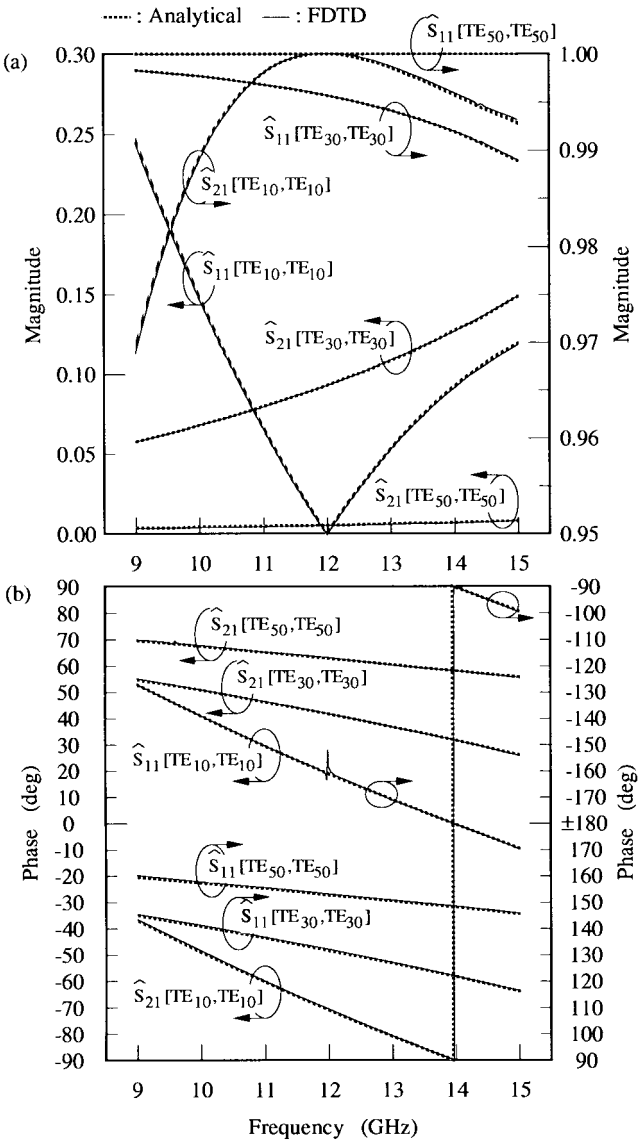

Fig. 6. The generalized scattering parameters of a hollow rectangular waveguide. (a) Magnitude. (b) Phase. Dimensions of the waveguide are $a = 19.05$ mm, $b = 9.525$ mm, and the length $l = 6.508$ mm. $\hat{S}_{11}$ and $\hat{S}_{21}$ when the both sides are terminated by 500 Ω are given. The FDTD simulation was done using a $76\Delta x \times \Delta y \times 20\Delta z$ mesh, where $\Delta x = 250.66$ μm, $\Delta y = 9.525$ mm, and $\Delta z = 325.4$ μm. $\Delta t = 417.763$ fs.

$S_{11}[\mathrm{TE}_{10}, \mathrm{TE}_{10}]$, and $S_{21}[\mathrm{TE}_{10}, \mathrm{TE}_{10}]$ are obviously zero and unity, respectively. However, $\hat{S}_{11}[\mathrm{TE}_{10}, \mathrm{TE}_{10}]$ is not zero and $\hat{S}_{21}[\mathrm{TE}_{10}, \mathrm{TE}_{10}]$ is not one, except for a point around 12 GHz, at which the characteristic impedance of this mode matches 500 Ω. Similarly, since the frequency region is below the cutoffs of TE_{30} and TE_{50} modes, the magnitudes of $\hat{S}_{11}[\mathrm{TE}_{30}, \mathrm{TE}_{30}]$ and $\hat{S}_{11}[\mathrm{TE}_{50}, \mathrm{TE}_{50}]$ are high, but are still not unity. These results can be obtained analytically as

$$[\hat{S}] = [G_{\hat{S}\leftarrow S}] \oplus [S] \oplus [G_{S\rightarrow\hat{S}}] \tag{44}$$

where

$$[S[\mathrm{TE}_{10}, \mathrm{TE}_{10}]] = \begin{bmatrix} 0 & e^{-\gamma_{\mathrm{TE}10}(\omega)l} \\ e^{-\gamma_{\mathrm{TE}10}(\omega)l} & 0 \end{bmatrix} \tag{45}$$

$$[G_{\hat{S}_{1,\mathrm{TE}_{10}}\leftarrow S_{1,\mathrm{TE}_{10}}}] = \begin{bmatrix} -\Gamma & (1+\Gamma)/\sqrt{R} \\ (1-\Gamma)\sqrt{R} & \Gamma \end{bmatrix} \tag{46}$$

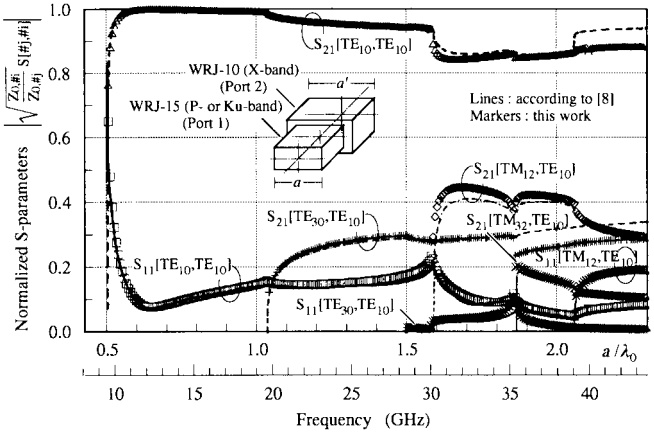

Fig. 7. Normalized scattering parameters of step discontinuity between two waveguides. The structure dimensions are $a = 15.8$ mm and $b = 7.9$ mm for WRJ-15 (P- or Ku-bands, 12.4–18 GHz) waveguide; $a' = 22.9$ mm and $b' = 10.2$ mm for WRJ-10 (X-band, 8.2–12.4 GHz) waveguide. Our results are compared with those after [8]. The mesh is $129\Delta x \times 71\Delta y \times 40\Delta z$, where $\Delta x = 177.528$ μm, $\Delta y = 143.636$ μm and $\Delta z = 200$ μm. $\Delta t = 239.393$ fs. Data are plotted in the frequency range where the concerned modes are propagating modes. The top nine modes in Table I were taken into account in this calculation.

$$[G_{S_{2,\mathrm{TE}_{10}}\rightarrow\hat{S}_{2,\mathrm{TE}_{10}}}] = \begin{bmatrix} \Gamma & (1-\Gamma)/\sqrt{R} \\ (1+\Gamma)\sqrt{R} & -\Gamma \end{bmatrix} \tag{47}$$

and

$$\Gamma(\omega) = \frac{R - Z_{0,\mathrm{TE}_{10}}(\omega)}{R + Z_{0,\mathrm{TE}_{10}}(\omega)} \tag{48}$$

for the TE_{10} mode, for instance. The results obtained by the new technique compare with the analytical results quite well as seen in these figures.

B. Step Discontinuity Between Two Rectangular Waveguides

The next structure for the verification is the step discontinuity between a WRJ-15 (P- or Ku-bands) waveguide and a WRJ-10 (X-band) waveguide [8], as shown in the inset of Fig. 7. When a wave in the TE_{10} mode is incident from port 1, TE_{mn}, and TM_{mn} modes, where m is odd and n is even in this case, can be excited due to the discontinuity. If an induced mode has the possibility of showing significant magnitudes at the reference planes, the mode should be considered in the calculation of modal expansion. However, on the other hand, since the computational effort increases in proportion to the number of modes, it is desirable to select the minimum set of modes that are required to characterize the component with a certain accuracy. $(M + N)$ FDTD simulations [$(M + N)$ iterations of steps (5)–(8) at the procedure described in the beginning of this section] are required in general if N and M modes are taken into account at the physical ports 1 and 2, respectively. In this example, we introduce a guideline for the mode selection [9], which utilizes quantities of power dissipation at the resistive ports.

The minimum set is not always found explicitly prior to the analysis. Let us take as many modes as possible for a preliminary set determined in step (2) of the S-parameter calculation procedure. In this example, choose the TE_{10}-mode

TABLE I
SELECTED MODES FOR THE EXAMPLE IN FIG. 7. RELATIVE $P_{\max}$ IS THE MAXIMUM POWER DISSIPATED AT THE MODAL PORT IN THE FREQUENCY RANGE OF INTEREST (10–40 GHz) WHEN THE PORT IS SELECTED. $f_{@\max}$ IS THE FREQUENCY AT WHICH P BECOMES MAXIMUM. f_c IS THE CUTOFF FREQUENCY OF THE MODE

No.	Mode	Rel. $P_{\max}$	$f_{@\max}$	f_c
1	TE_{10}(P-band)	-	-	9.49GHz
2	TE_{10}(X-band)	0.97706	12.11GHz	6.55GHz
3	TM_{12}(X-band)	0.19067	32.13GHz	30.13GHz
4	TE_{30}(X-band)	0.08447	32.64GHz	19.65GHz
5	TM_{32}(X-band)	0.03612	35.57GHz	35.37GHz
6	TE_{30}(P-band)	0.01060	35.31GHz	28.48GHz
7	TM_{12}(P-band)	0.02426	39.90GHz	39.14GHz
8	TE_{12}(X-band)	0.01043	35.44GHz	30.13GHz
9	TE_{12}(P-band)	0.00388	35.31GHz	39.14GHz
10	TE_{50}(X-band)	0.00512	35.44GHz	32.75GHz
11	TE_{32}(X-band)	0.00282	39.14GHz	35.37GHz
12	TM_{52}(X-band)	0.00049	35.31GHz	44.02GHz
13	TM_{32}(P-band)	0.00023	35.31GHz	47.47GHz
14	TM_{14}(X-band)	0.00004	39.90GHz	59.19GHz
15	TE_{52}(X-band)	0.00003	35.31GHz	44.02GHz

of the WRJ-15 waveguide as the #1 mode, which is a fundamental mode, and execute the first FDTD simulation. We then obtain $\hat{S}_{11}[\#i,\#1]$ and $\hat{S}_{21}[\#j,\#1]$, where $i = 1,2,\cdots,M$ and $j = 1,2,\cdots,N$. These parameters constitute a column vector $\{\hat{S}[\#k,\#1], k = 1, M+N\}^T$, which corresponds to the first column of preliminary $M+N$ port S-matrix $[\hat{S}]$. Now consider a new matrix given by

$$[G_{S_{\#1}\leftarrow\hat{S}_{\#1}}] \oplus [\hat{S}]. \tag{49}$$

This operation deembeds the imposed terminating condition from modal port #1. The first column of deembedded matrix $\{S'[\#1,\#1], (\hat{S}'[\#k,\#1], k = 2, M+N)\}^T$ can be calculated from previously obtained parameters according to formulas similar to (14) and (16). Using these components, evaluate

$$P(k,\omega) = Z_{0,\#1}(\omega)\hat{S}'[\#k,\#1](\omega)\hat{S}'^{*}[\#k,\#1](\omega) \tag{50}$$

for each k, where $2 \le k \le M+N$. Find the port number k that gives the maximum value of P in the frequency range of interest. Select the port $\#k$ as the excitation port in the next simulation. Equation (50) represents the relative power that is dissipated at the kth modal port if a unit wave is incident from port $\#1$. In the next selection, two ports are deembedded before evaluating the values of P. In this way, we can select the modes that are to be considered. Table I shows the order of selected modes. The value of $P_{\max}$ may be used as a criteria for truncating the number of modes. Fig. 7 presents results obtained, taking the top nine modes into account, which compare well with the results after [8].

V. APPLICATIONS

A. Unsymmetrical Resonant Iris

Let us present two examples of the hybrid analysis based on the generalized scattering matrix. The first one is an unsymmetrical resonant iris in the WRJ-15 waveguide [8] in

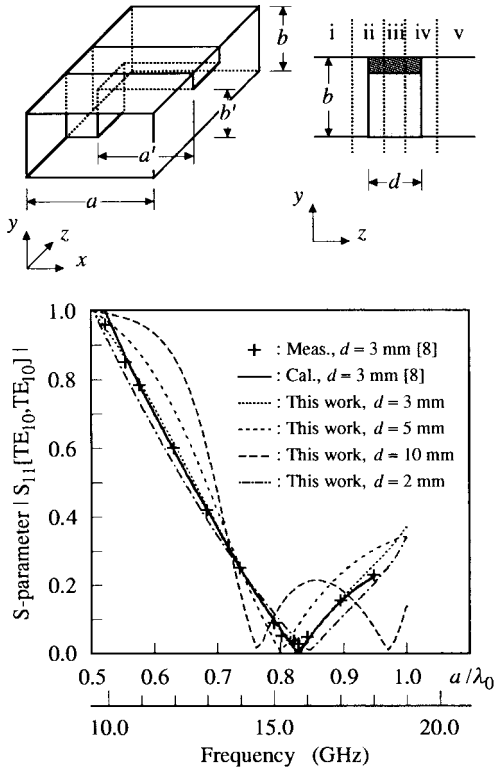

Fig. 8. Magnitude of the reflection coefficient of an unsymmetrical resonant iris. $a = 15.8$ mm, $b = 7.9$ mm, $a' = 11.85$ mm, and $b' = 6$ mm. The structure was divided into five parts. Parts ii and/or iv (both are identical) are analyzed using FDTD with a $120\Delta x \times 79\Delta y \times 20\Delta z$ mesh, where $\Delta x = 131.667$ μm, $\Delta y = 100$ μm, and $\Delta z = 100$ μm. $\Delta t = 166.667$ fs.

Fig. 8. In order to demonstrate the synthesis by the generalized scattering matrix, we divided the structure into five parts. The matrix of parts ii and iv (these are symmetrical) was calculated by the FDTD simulations using the presented new technique. Other matrices were prepared analytically, as previously shown in the section of a hollow waveguide. The composite matrix of the total structure was then synthesized by

$$[\overline{S}] = [S_{\mathrm{i}}] \oplus [G_{S\leftarrow\hat{S}}] \oplus [\hat{S}_{\mathrm{ii}}] \oplus [\hat{S}_{\mathrm{iii}}] \oplus [\hat{S}_{\mathrm{iv}}] \oplus [G_{\hat{S}\rightarrow S}] \oplus [S_{\mathrm{v}}]. \tag{51}$$

Ten modes (TE_{10}, TE_{20}, TM_{11}, TE_{30}, TE_{11}, TM_{12}, TE_{21}, TM_{21}, TE_{12}, and TM_{22}) in the WRJ-15 waveguide region and four modes (TE_{10}, TE_{20}, TM_{11}, and TE_{11}) in the iris were selected in the frequency range of 10–18 GHz and considered in the calculation based on the similar mode-selection procedure described in the previous section. Fig. 8 plots the frequency characteristics of the reflection coefficient $S_{11}[\mathrm{TE}_{10}, \mathrm{TE}_{10}]$ with the thickness of iris d as a parameter. Thickness d can be varied at once so that only part iii needs to be replaced. Measured and calculated data after [8] are also plotted, which agree well with our results.

B. E-Plane Waveguide Filter with Metal Fins

Fig. 9 shows an analysis of an E-plane bandpass filter having three metal fins (inductive posts) in a rectangular waveguide. In this case, the whole structure was divided into

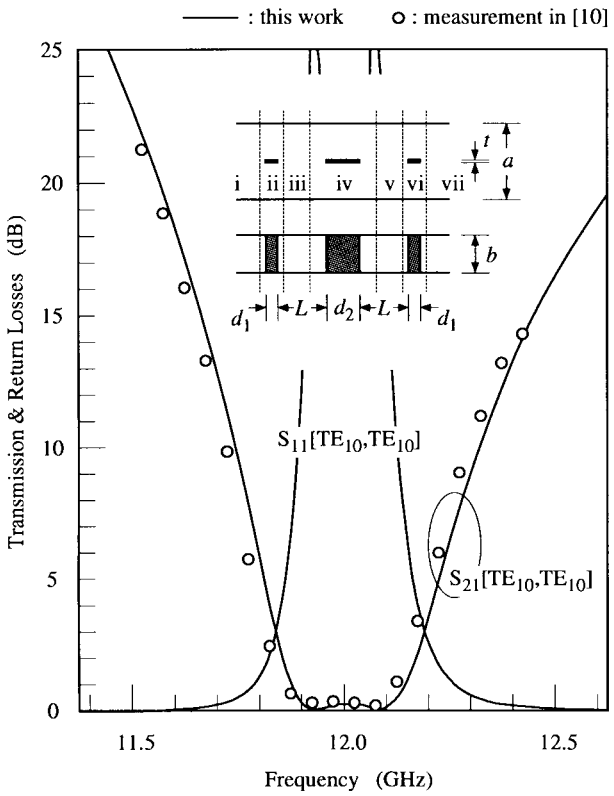

Fig. 9. Transmission and return losses of a rectangular waveguide E-plane filter [10]: $a = 19.05$, $b = 9.525$,$t = 0.50$,$d_1 = 2.976$,$d_2 = 8.554$, $L = 12.273$. Dimensions are all in millimeters. The mesh sizes of $76\Delta x \times \Delta y \times 20\Delta z$ for parts ii or vi and $76\Delta x \times \Delta y \times 40\Delta z$ for part iv were used, where $\Delta x = 250.66$ μm and $\Delta y = 9.525$ mm. $\Delta z = 297.6$ μm for parts ii/vi and 427.7 μm for part iv. $\Delta t = \Delta x/2c$. A compensation technique for conductor edge singularities [11] is used in the FDTD simulations.

seven parts. The matrices of parts ii, iv, and vi were then calculated by the FDTD. The rest were obtained analytically. Finally, the composite matrix was calculated as

$$[\overline{S}] = [S_{\rm i}] \oplus [G_{S \leftarrow \hat{S}}] \oplus [\hat{S}_{\rm ii}] \oplus [\hat{S}_{\rm iii}] \oplus [\hat{S}_{\rm iv}] \oplus [\hat{S}_{v}] \oplus [\hat{S}_{vi}] \oplus [G_{\hat{S} \rightarrow S}] \oplus [S_{\rm vii}]. \quad (52)$$

The result is presented in the figure, and it agrees well with measured data [10]. In this result, the lowest five modes, i.e., $\rm TE_{10}$, $\rm TE_{30}$, $\rm TE_{50}$, $\rm TE_{70}$, and $\rm TE_{90}$ modes are taken into account. However, taking the lowest three modes would be sufficient for this particular example.

If we compare the hybrid analysis with the single FDTD analysis of a whole structure, one can see that the former has the following merits.

1) By dividing a whole structure into N parts, the scale of each analysis roughly decreases to $1/N$. This reduces the computer memory requirement or makes the analysis of more complex structures possible.
2) Some of divided parts may be characterized analytically, as demonstrated in the previous section. This increases the total efficiency of the analysis.
3) A structure may be divided nicely so that some components become symmetrical or identical, as seen in our examples. We can build and reuse the matrix database for frequently appearing components.
4) Since the analysis of each component is completely independent, total analysis can be speeded up by using many computers in parallel. Even step (9) of the procedure may be carried out in parallel.
5) Due to this independence, the descretization length of each part can be selected arbitrarily. This allows more freedom for precise representation of the structure.
6) Since each component does not have high-Q resonance by itself in the case of the E-plane filter example, the time-stepping in the FDTD analysis can be terminated much earlier than that of the whole structure. This is a significant advantage that should be emphasized regarding time-domain techniques.
7) Finally, sensitivity analysis of some structure dimensions becomes easy, as demonstrated in the iris example with parameter d.

VI. Conclusions

This paper presented a hybrid-analysis method for metal waveguide circuits. The method is based on the generalized-scattering-matrix approach. A new technique was introduced for the FDTD modeling of waveguide components. In the FDTD simulation, the IBC is used for the port termination instead of complicated ABC's, and the generalized scattering matrix is calculated from nodal voltages of modal ports. Therefore, some troublesome procedures required in the conventional technique are avoidable, and rigorous analysis can be performed efficiently. Though we demonstrated the utility of the method using relatively simple conventional examples, the substantial advantage of this hybrid method is its ability to deal with arbitrarily shaped structures. The method is expected to be used in efficient analyses of larger and more complex structures.

References

[1] G. F. Vanblaricum, Jr. and R. Mittra, "A modified residue-calculus technique for solving a class of boundary value problems," *IEEE Trans. Microwave Theory Tech.*, vol. MTT-17, pp. 302–319, June 1969.
[2] R. Mittra and S. W. Lee, *Analytical Techniques in the Theory of Guided Waves*. New York: Macmillan, 1971, pp. 207–217.
[3] T. W. Huang, B. Houshmand, and T. Itoh, "Efficient modes extraction and numerically exact matched sources for a homogeneous waveguide cross-section in a FDTD simulation," in *IEEE MTT-S Int. Microwave Symp. Dig.*, San Diego, CA, May 23–27, 1994.
[4] M. Righi, W. J. R. Hoefer, M. Mongiardo, and R. Sorrentino, "Efficient TLM diakoptics for separable structures," *IEEE Trans. Microwave Theory Tech.*, vol. 43, pp. 854–859, Apr. 1995.
[5] F. Alimenti, P. Mezzanotte, L. Roselli, and R. Sorrentino, "Analysis of planar circuits with a combined 3-D FDTD-time domain modal expansion method," in *IEEE MTT-S Int. Microwave Symp. Dig.*, San Francisco, CA, June 18–20, 1996.
[6] T. Shibata, Y. Qian, and T. Itoh, "An FDTD impedance boundary condition and its application to waveguide discontinuity analyses," in *IEEE MTT-S Int. Microwave Symp. Dig.*, Denver, CO, June 8–13, 1997.
[7] T. Shibata and H. Kimura, "Computer-aided engineering for microwave and millimeter-wave circuits using the FD-TD technique of field simu-

lations," *Int. J. Microwave Millimeter-Wave Computer-Aided Eng.*, vol. 3, pp. 238–250, July 1993.

[8] H. Patzelt and F. Arndt, "Double-plane steps in rectangular waveguides and their application for transformers, irises, and filters," *IEEE Trans. Microwave Theory Tech.*, vol. MTT-30, pp. 771–776, May 1982.

[9] T. Shibata and T. Itoh, "Frequency domain diakoptics for IC packaging structures based on the PEE and FDTD methods," *IEICE Trans. Electron.*, vol. E81-C, pp. 801–809, June 1998.

[10] Y. Tajima and Y. Sawayama, "Design and analysis of a waveguide-sandwich microwave filter," *IEEE Trans. Microwave Theory Tech.*, vol. MTT-22, pp. 839–841, Sept. 1974.

[11] T. Shibata and T. Itoh, "A modification of FDTD formulas at conductor edge singularities," *IEICE Trans. Electron.*, vol. J80-C-I, pp. 248–249, May 1997.

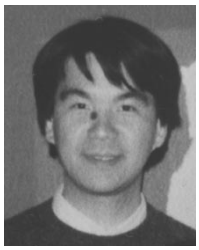

Tsugumichi Shibata (M'87) graduated from the Tokyo National College of Technology, Tokyo, Japan, in 1980. He received the B.S., M.S., and Ph.D. degrees in electrical engineering from the University of Tokyo, in 1983, 1985, and 1995, respectively.

In 1985, he joined the Atsugi Electrical Communications Laboratories, Nippon Telegraph and Telephone (NTT) Corporation, where he has been engaged in research on computer-aided design (CAD) applications of electromagnetic-field analysis, electrooptic sampling of subpicosecond signals in integrated circuit (IC) chips, and the design of high-speed devices and circuits for data transmission systems. He was a Visiting Scholar at the University of California at Los Angeles (UCLA), from 1996 to 1997. He is currently a Senior Research Engineer and Supervisor at NTT System Electronics Laboratories, Atsugi, Japan.

Dr. Shibata is a member of the Institute of Electronics, Information and Communication Engineers (IEICE), Japan.

Tatsuo Itoh (S'69–M'69–SM'74–F'82–LF'94) received the B.S. and M.S. degrees from Yokohama National University, Kanagawa, Japan, in 1964, and 1966, respectively, and the Ph.D. degree in electrical engineering from the University of Illinois at Urbana-Champaign, in 1969.

From 1966 to 1976, he was with Electrical Engineering Department, University of Illinois at Urbana-Champaign. From 1976 to 1977, he was a Senior Research Engineer in the Radio Physics Laboratory, SRI International, Menlo Park, CA. From 1977 to 1978, he was an Associate Professor at the University of Kentucky, Lexington. In July 1978, he joined the faculty at the University of Texas at Austin, where he became a Professor of electrical engineering in 1981, and Director of the Electrical Engineering Research Laboratory in 1984. During the summer of 1979, he was a Guest Researcher at AEG-Telefunken, Ulm, Germany. In 1983, he was selected to hold the Hyden Head Centennial Professorship of Engineering at the University of Texas. In 1984, he was appointed Associate Chairman for research and planning of the Electrical and Computer Engineering Department, University of Texas. In 1991, he joined the University of California at Los Angeles (UCLA), as Professor of electrical engineering, and became the Holder of the TRW Endowed Chair in microwave and millimeter-wave electronics. He is currently the Director of the Joint Services Electronics Program (JSEP), and Director of the Multidisciplinary University Research Initiative (MURI) Program at UCLA. He has been an Honorary Visiting Professor at Nanjin Institute of Technology, China, as well as at the Japan Defense Academy. In 1994, he was made an Adjunct Research Officer for the Communications Research Laboratory, Ministry of Post and Telecommunication, Japan. He currently holds a Visiting Professorship at the University of Leeds, U.K., and is an External Examiner of the graduate program of the City University of Hong Kong. He serves on advisory boards and committees of a number of organizations, including the National Research Council and the Institute of Mobile and Satellite Communication, Germany. He was the chairman of USNC/URSI Commission D (1988–1990), the vice chairman of Commission D of the International URSI (1991–1993), and chairman of the same commission (1994–1996). Since 1996, he has been on the Long Range Planning Committee of URSI.

Dr. Itoh is a member of the Institute of Electronics, Information and Communication Engineers (IEICE), a member of Commissions B and D of USNC/URSI, and was elected an honorary life member of the IEEE Microwave Theory and Techniques Society (MTT-S) in 1994. He served as the editor of IEEE TRANSACTIONS ON MICROWAVE THEORY AND TECHNIQUES (1983–1985), and editor-in-chief of the IEEE MICROWAVE AND GUIDED WAVE LETTERS (1991–1994). He also serves on the administrative committee of IEEE MTT-S. He was vice president of the Microwave Theory and Techniques Society (1989) and president (1990).